

Coarse-to-Fine Registration of Airborne LiDAR Data and Optical Imagery on Urban Scenes

Thanh Huy Nguyen, *Student Member, IEEE*, Sylvie Daniel, *Senior Member, IEEE*, Didier Guriot, *Senior Member, IEEE*, Christophe Sints, *Senior Member, IEEE* and Jean-Marc Le Caillec, *Senior Member, IEEE*

Abstract—Applications based on synergistic integration of optical imagery and LiDAR data are receiving a growing interest from the remote sensing community. However, a misaligned integration between these datasets may fail to fully profit from the potential of both sensors. In this regard, an optimum fusion of optical imagery and LiDAR data requires an accurate registration. This is a complex problem since a versatile solution is still missing, especially when considering the context where data are collected at different times, from different platforms, under different acquisition configurations. This paper presents a coarse-to-fine registration method of aerial or satellite optical imagery with airborne LiDAR data acquired in such context. Firstly, a coarse registration involves processes of extraction and matching of building candidates from LiDAR data and optical imagery. Then, a Mutual Information-based fine registration is carried out. It involves a super-resolution approach applied to LiDAR data to generate images with the same resolution as the optical image, and a local approach of transformation model estimation. The proposed method succeeds at overcoming the challenges associated with the aforementioned difficult context. For instance, considering the experimented airborne LiDAR (2011) and orthorectified aerial imagery (2016) datasets, their spatial shift is reduced by almost a half (i.e. 48.15%) after the proposed coarse registration. Moreover, the incompatibility of size and spatial resolution is well addressed by the mentioned super-resolution approach. Finally, a high accuracy of dataset alignment is also achieved, highlighted by a 40-cm error based on a check-point assessment and a 64-cm error based on a check-pair-line assessment. Promising results yielded by this registration enable further research for a complete versatile fusion methodology between airborne LiDAR and optical imagery data in this challenging context.

Index Terms—Airborne LiDAR, optical imagery, aerial imagery, satellite imagery, registration, heterogeneous sensors, multimodal, coarse-to-fine, building extraction, super-resolution, mutual information, urban scene.

I. INTRODUCTION

THE perception of an environment on the Earth's surface and follow-up exploitations require using multiple sensors to capture specific and complementary characteristics of this environment [1], [2]. In many areas of remote sensing, observations from heterogeneous sources are coupled and jointly analyzed to achieve a richer description of a scene. This can be done by mutually benefiting from their strengths

and reducing the data uncertainty and incompleteness relating to each sensor [3]–[6]. As a matter of fact, the fusion of multi-source data has become one of the mainstream research topics in the exploitation of remote sensing data nowadays [2], [7].

Light Detection And Ranging (LiDAR) and photogrammetry systems are major sources for fast and reliable spatial data acquisition. They provide data that are complementary to each other while the two systems differ fundamentally in their operation and data collection principles. The first one is an active sensor while the second is passive. On the one hand, airborne LiDAR systems are widely used for providing accurate three-dimensional (3-D) surface information and 3-D geometry of objects and ground elements, in the modality of scattered point clouds (recorded according to range detection principle) [8]. On the other hand, aerial and satellite photogrammetry supplies rich semantic and texture information, in the form of multispectral images [9]. By integrating the two technologies, many applications have been enabled such as building extraction [4], [10], city digital twin construction [11], land use and land cover classification [12] and so on.

A. Motivation

Over the years, existing works in the domain of data fusion between optical imagery and airborne LiDAR data have addressed dedicated acquisition contexts, in which the respective image and the LiDAR 3-D point cloud are already registered and/or they are acquired from the same platform at identical or very close dates. For instance, solutions submitted to the 2013 Data Fusion Contest of the IEEE Geoscience and Remote Sensing Society (GRSS) [13] focused on the fusion between LiDAR data and hyperspectral imagery with the same spatial resolution, acquired on two consecutive days. The same contest in 2015 [14], [15] involved extremely high resolution LiDAR data and RGB imagery collected from the same airplane with the sensors being rigidly fixed to the same platform. In other words, the solutions submitted to these contests, as well as many others, e.g. [16]–[18], have not intended to cope with the inherent obstacles of the context where datasets are collected from different platforms with different acquisition configuration (e.g. different flying track, height, orientation, and so on) at different moments and even in different seasons, with different spatial resolutions and levels of detail.

This research work aims to propose a relevant registration method in this context. Table I summarizes the specifications of the sensors as well as their platforms considered in this

T. H. Nguyen is with the Department of Geomatics, Universit Laval, Quebec City, QC G1V 0A6, Canada, and also with IMT Atlantique, Lab-STICC, UMR CNRS 6285, F-29238 Brest, France (e-mail: thanh.nguyen@imt-atlantique.fr).

S. Daniel is with the Department of Geomatics, Universit Laval, Quebec City, QC G1V 0A6, Canada.

D. Guriot, C. Sints and J.-M. Le Caillec are with IMT Atlantique, Lab-STICC, UMR CNRS 6285, F-29238 Brest, France.

paper. The need for a relevant registration in such a crucial context is exemplified in the work undertaken by Cura *et al.* [19]. It also relates to the rise of the availability of data captured by different heterogeneous sensors that requires an efficient integration [7]. However, a solution that is versatile enough to overcome this difficult context still remains an unsolved research problem [20].

B. Challenges

The development of a relevant registration approach in this unresolved context faces many challenges.

1) *Spatial shift between datasets*: The first challenge relates to the differences between the dataset point of view and field of view, which lead to a significant spatial shift between them. For instance, a spatial shift exists approximately 1-2 meters between orthorectified airborne imagery (2016) and LiDAR data (2011), or up to 40 meters between Pliades imagery and LiDAR data (2011). According to our literature review, a coarse registration, which is necessary to reposition the two datasets, has not been rigorously studied by existing works. This step is often bypassed using the dataset geospatial coordinates provided by a GPS/IMU system [11], [18], [21].

2) *Uncertainty, imprecision and incompleteness*: Distortions in the information extracted from optical images can be caused by radiometric errors like sensor sensibility, illumination changes, atmospheric effects, and geometric errors such as relief displacement, occlusions or shadows [22]. On the other hand, points may be missing in the LiDAR data due to occlusion or presence of water [23]. These errors, distortions and missing data from each of the two datasets induce incompleteness, imprecisions and uncertainties within the registration and fusion processes of these data [24].

3) *Spatial resolution and level of detail*: There are significant differences in spatial resolution and level of detail between the airborne or satellite imagery and LiDAR data. They cause the scene elements and objects to appear very differently within the datasets. Thus, the determination and extraction of corresponding landmarks is complex.

4) *Relevance of registration features*: The nature of a scene, either in urban or natural environment, conditions strongly the entities within the datasets that would be relevant to perform the registration [25].

5) *Accuracy of dataset registration*: When performing the fusion of airborne LiDAR data and optical imagery, even a small misalignment between them can lead to an unfavorable impact on the quality of the integrated product, or a significant reduction of data information content [26]. Thus, an accuracy of 1-pixel is recommended for the data set registration [17]. As a matter of fact, a *sub-pixel level* of accuracy, assessed by measuring the distances between control points, is usually preferred for a *good* registration. However, such a qualitative criterion is difficult to achieve because the image pixel resolution can vary from several dozens of centimeters to several meters depending on the platform (i.e. airborne versus satellite). Current works in the literature involve resulting discrepancies between the registered datasets ranging from 45 centimeters to 50 centimeters [16], [27]. They state that such discrepancies are a decent and desirable registration accuracy.

C. Contribution

This paper addresses the need for a versatile and relevant registration approach able to overcome the aforementioned challenges. The versatility of our proposed method is reflected through its capability of registering the datasets that are not acquired simultaneously, nor from the same platform and same acquisition configuration, nor having same spatial resolution. These assumptions are crucial to the existing works [16]–[18]. In this regard, we propose a coarse-to-fine registration approach.

- Firstly, a coarse registration is performed to reposition the datasets closer to each other. It addresses the challenge of spatial shift between datasets which is problematic but usually overlooked. In this paper, we present a building-based coarse registration.
- Secondly, a fine registration is carried out based on a local transformation model estimation. This fine registration is enabled by a super-resolution approach applied to LiDAR data in order to generate images with the same resolution as the optical image. This approach is devoted to overcome the hindering caused by the spatial resolution difference between datasets.

A coarse-to-fine approach is necessary in order to register an airborne LiDAR dataset with an optical image. The mentioned coarse registration aims to reposition the two datasets in a fast but reliable manner. As a result, a global transformation model is estimated, composed of a set of coarsely estimated camera pose parameters. Even though the global transformation does not permit the dataset to be precisely registered, it narrows down the search space for optimal camera pose parameters from an initial set of values during the fine registration. However, the main drawback of this feature-based approach is that the building primitives are not distributed evenly throughout the datasets. Hence, the global transformation has the tendency to prioritize a region exhibiting more primitives than others. Therefore, we propose a subsequent fine registration that focuses on determining the optimal parameters for each local region of the considered urban area. Such a local approach brings two benefits, namely a higher registration accuracy and a reduced computational cost of this fine registration. Then, we also propose a refinement of locally optimized transformation models, in order to avoid conflicts between them. Lastly, the proposed method relies on tailored series of well-known processes and algorithms while avoiding complicated and labor-intensive processes.

D. Paper organization

The remainder of this paper is structured as follows: a brief review of existing works related to the registration of optical imagery and airborne LiDAR data is provided in Section II. Then, Section III presents the proposed methodological approach, consisting of two parts: coarse then fine registration. Then, multiple quantitative assessments involving different datasets are presented and discussed in Section IV. Finally, Section V provides conclusions and perspectives of this work.

TABLE I
SENSOR AND PLATFORM SPECIFICATIONS.

	Optical imagery		LiDAR data	
	Aerial image (2016)	Satellite image (2015)	Airborne LiDAR (2017)	Airborne LiDAR (2011)
Principle	Passive	Passive	Active	Active
Device (Camera/LiDAR) - Platform	Vexcel UltraCAM Xp - Piper Navajo	Pliades HR	Optech ALTM Galaxy - Piper Aztec	Optech ALTM Gemini - Piper Navajo
Sensor design	Time-Delay Integration Camera	Pushbroom	Whiskbroom	Whiskbroom
Acquisition dates (season)	June 2016 (summer)	June 2015 (summer)	May-June 2017 (summer)	Oct.-Nov. 2011 (winter)
Flying height	2955 m	695 km	1300 m	950 m
Swath width	2597 m (cross-track) 1697 m (along-track)	20 km	946 m	620 m
Field-Of-View (FOV)	55° (cross-track) 37° (along-track)		20°	20°
Instantaneous Field-Of-View (IFOV)	0.17 mrad (cross-track) 0.17 mrad (along-track)	1 μ rad (PAN) 4 μ rad (MS)	-	-
Focal length	100.5 mm	-	-	-
Number of orbits per day	-	14+15/26	-	-
Nominal repeat cycle	-	26 days	-	-
Laser repetition rate	-	-	350 kHz	100 kHz
Scan frequency	-	-	70 Hz	50 Hz
Laser beam divergence	-	-	0.25 mrad	0.25 & 0.8 mrad
Spectral bands/ Laser wavelength	R, G, B, NIR	470-830 nm (PAN) R, G, B, NIR (MS)	1064 nm	1064 nm
Number of returns per pulse	-	-	4	4
Point density	-	-	8 points/m ²	2 points/m ²
Point spacing	-	-	35.4 cm	70 cm
Point classification	-	-	U, G, Lv, Mv, Hv, B ¹	U, G, Lv, Mv, Hv
Ground sample distance	15 cm	50 cm (PAN), 2 m (MS)	-	-
Laser beam footprint size	-	-	33 cm	23 cm
Lateral overlapping	35%	-	65 %	30%
Longitudinal overlapping	60%	-	-	-
Theoretical horizontal accuracy (RMSE)	13-16.5 cm (at perspective centers), 4-5.5 cm (at control points) after <i>Aerotriangulation</i>	1 m (with ground control points) and 3 m (without ground control points)	1/7500 \times Altitude, i.e. \approx 17 cm	1/5500 \times Altitude, i.e. \approx 17 cm
Theoretical elevation accuracy (RMSE)	-	-	3-20 cm	5-35 cm

¹Classification of LiDAR point cloud is: unclassified (U), ground (G), low vegetation (Lv), medium vegetation (Mv), high vegetation (Hv) and building (B).

II. LITERATURE REVIEW

Accurate registration of LiDAR data and optical imagery is the crucial prerequisite to any data fusion applications using them [16], [28]. The majority of automatic methods for registering such datasets can be classified into two categories, namely area-based and feature-based methods [29]. On the one hand, area-based methods determine the optimal pose of camera by maximizing a statistical similarity, e.g. Mutual Information (MI), between the values of image pixels and of LiDAR-derived image pixels [11], [17], [30]–[34]. The LiDAR-derived image is either a Digital Surface Model (DSM), an intensity image, or an image of *pdet* (probability of detection) attributes derived from the LiDAR point cloud [11]. Their main drawbacks, in addition to being computationally costly, are the necessities for the datasets to be spatially close to each other, as well as to have the same resolution and display similar intensity characteristics. For instance, the similarity of characteristics between two-dimensional (2-D) images and normals to a 3-D surface is shown to be important for area-based registration methods [35].

On the other hand, feature-based methods establish correspondence between datasets based on available distinguishable features. They involve feature extraction algorithms and feature matching strategy [36]–[41]. The employed features can be either from built environment, such as corner points,

break lines and planar surfaces found in man-made objects, or natural features like trees, bushes and ground surface features. However, features from built environment usually lead to higher accuracy result than natural features [37].

Wong and Orchard [40] proposed a registration method between LiDAR data and optical image, considering they are two images of the same resolution. From LiDAR data, it is an image of laser return intensity data. This method consists in using a modified Harris corner detector to extract control points from the two images. Then, a Fast Fourier Transform-accelerated exhaustive search for correspondences among all extracted control points is carried out. However, this method fails to produce accurate registration result in the case of very high resolution images, according to [25]. Palenichka and Zaremba [41] proposed a registration method between LiDAR-derived DSM and optical imagery. It involves an automatic extraction of salient points from both the DSM and the optical image that allows the discrimination of the objects of interest from the background. This method facilitates the automatic selection of control points that also works on natural scenes. According to [25], the high computational cost and the lack of concern for relief shift are the drawbacks of this method. Liu *et al.* [27] proposed a registration method between airborne LiDAR data and UAV (Unmanned Aerial Vehicle) remote sensing imagery, based on 3-D and 2-D line segments

respectively from the LiDAR point cloud and the image. 2-D line segments are semi-automatically extracted from a localization on the image that exhibits a 3-D line segment. Then, a manual selection for conjugated line segments (i.e. the correspondences) is carried out. This method does not account for a spatial shift between the datasets. Therefore, it works on the datasets with a small spatial shift, but it may fail for large spatial shifts.

Many studies proposed to use different features to increase the registration accuracy. For example, Huang *et al.* [39] proposed a registration method using two different features at two scales, i.e. a line network of roads extracted using k -means clustering at the first scale, and building corners at the finer scale. However, the use of k -means clustering as an unsupervised classification on aerial images is seemingly too simple to extract roads effectively. Ding *et al.* [38] performed a coarse-to-fine approach to register oblique aerial image and LiDAR data based on vanishing points estimated from parallel vertical building edges at the coarse level, and then based on building corners at the fine level. While vertical vanishing points can be estimated using oblique images, this can hardly be done using vertical aerial and satellite images, as well as orthorectified images. A similar coarse-to-fine approach is also proposed by the authors of [16] to register hyperspectral image and LiDAR data simultaneously acquired, from the same airplane. First, Scale-Invariant Feature Transform [42] keypoint detector is used to determine tie points between the LiDAR data and hyperspectral image. Then, instead of using another feature, an area-based optimization is carried out to find optimal camera pose parameters. Within a small range from the values coarsely estimated using the tie points, these parameters are then refined by minimizing a cost function. The cost function is zero-mean sum squared distances calculated between pixels of the hyperspectral image and pixels of the image generated from LiDAR intensity data using a ray-tracing module.

All the methods reviewed in this section assume that the airborne LiDAR data and imagery are spatially close to each other, have been recorded simultaneously (or on very close dates) and have similar spatial resolution and level of details. To the best of our knowledge, a method explicitly devoted to the registration of LiDAR and image datasets acquired from two different platforms, with different configurations at different times and even seasons has not yet been proposed. In what follows, we expose our method to achieve such purposes.

III. PROPOSED METHOD

Fig. 1 presents the full flowchart of the proposed method. Firstly, the coarse registration approach is presented. Its purpose is to reposition the two datasets based on the extraction and matching of building candidates. Based on these primitives, a global transformation model is estimated, which is represented by a set of camera pose parameters, denoted by θ_{global} . Secondly, a fine registration based on super-resolutions (SR) of LiDAR values and an area-based optimization is carried out. The SR process takes into account a transformation model (i.e. θ_{global} at the first iteration) and generates high-resolution LiDAR-based images. Next, a statistical similarity

measure, namely Mutual Information (MI) or Normalized Combined Mutual Information (NCMI), between these super-resolved images and the optical image is estimated. Therefore, the estimated MI (or NCMI) value can be considered as a function of the transformation model. The maximum value of such measures is expected to be achieved when the images (i.e. the optical image and the super-resolved LiDAR-based images) are geometrically aligned [17]. As a result, an optimal transformation model associated to this maximum MI (or NCMI) value is determined. We detail the two registrations in the following two sub-sections.

A. Coarse Registration

Fig. 2 sums up the proposed coarse registration, which has been originally introduced in our previous work [43]. Man-made structures in urban scenes like buildings are more suitable for accurate registration, compared to natural features [37]. In addition, they remain unchanged through a relatively long period of time (e.g. several years). In airborne LiDAR datasets, the point density around vertical surfaces like building faades can be low. Hence, the localization accuracy of features like building corners and edges is deficient. As a result, our coarse registration method relies on region-based primitives namely buildings.

Thus, different series of processing steps are applied to the LiDAR and optical image datasets respectively in order to extract buildings. On the one hand, we apply a series of processing steps starting with an elevation thresholding on LiDAR point cloud. On the other hand, mean shift segmentation [44] is performed on the optical image with a contextually chosen bandwidth parameter. Further processing is then applied to remove unwanted segments and preserve building-like ones. The respective process of building extraction from the LiDAR point cloud and the optical image are described in III-A1 and III-A2. Then, the building candidates from each dataset are matched and yield a set of correspondences (III-A3), which feeds the estimation of a global transformation model (III-A4).

1) *Building extraction from LiDAR data:* The extraction of building regions from LiDAR point cloud is carried out through a series of steps. The results of many of these steps are depicted in Fig. 3. First, non-ground points are separated from ground points using an elevation thresholding. This thresholding is proposed by many existing works as a necessary initial step [45]. The threshold is set as follows, $T_e = H_g + T_{r,f}$, where H_g denotes the ground elevation and $T_{r,f}$ is a relief factor. The first value H_g , as proposed by [45], can be determined from a Digital Terrain Model (DTM) generated from the LiDAR point cloud data [46]. Otherwise, since the LiDAR point cloud contains information of the point classification (as described in Table I), we can also measure H_g by the average elevation of ground points, i.e. $H_g = \text{mean}(z_g)$ where z_g represents the elevation of ground points. The second value $T_{r,f}$ is empirically set to $T_{r,f} = 2.5$ meters (usual minimum height of a building).

All non-ground points are then vertically projected onto the plan $z = 0$. A raster grid representing these projected points is created (Fig. 3a). The resolution of the grid is set according to

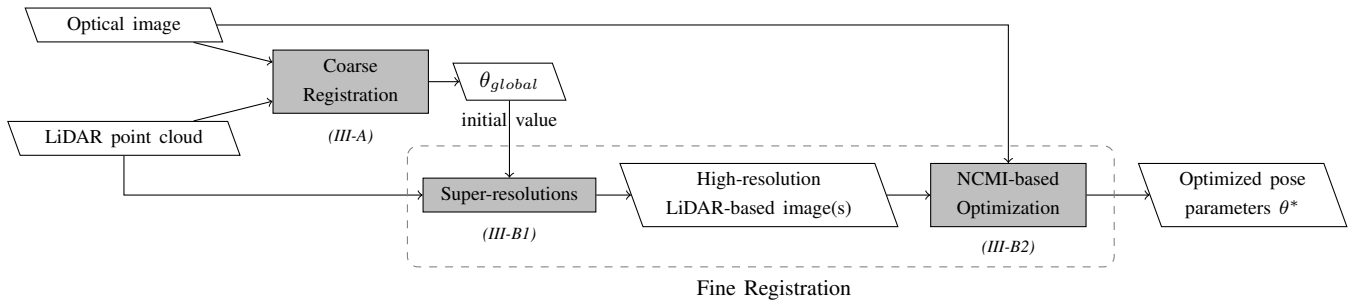


Fig. 1. Flowchart of the registration of optical imagery and airborne LiDAR data (NCMI: Normalized Combined Mutual Information). A parenthesis below each procedure block denotes their respective descriptive sub-section in this paper.

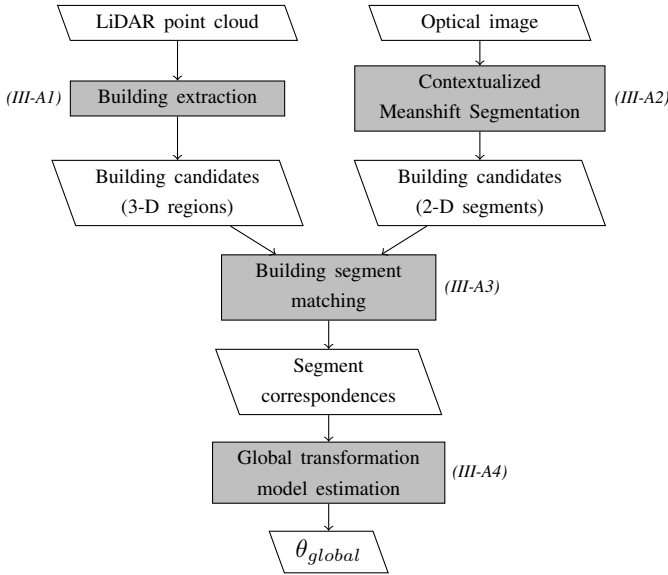


Fig. 2. Flowchart of the building-based coarse registration between optical image and LiDAR point cloud. A parenthesis next to each procedure block denotes their respective descriptive sub-section in this paper.

the LiDAR point cloud density, in order to avoid null-valued pixels. For instance, for the LiDAR data (2011) with 70 cm of point spacing, the resolution of the grid is set to 1 meter. A binary grid of same resolution is also generated. Its cell value is set to 1 or 0 according to the presence or absence of projected non-ground points in the cell ('1': presence, '0': absence). Then, a morphological opening operator is applied to remove small artifacts on the binary grid, resulting Fig. 3b. Remaining grid cells with value set to 1 are grouped into labeled segments based on their connectivity. Next, small segments (e.g. smaller than 10 square meters) are removed. The resulting grid consists of a number of relatively large labeled segments related to buildings (Fig. 3c). These segments are then used to select the building points in the LiDAR point cloud. A convex hull is calculated on each set of these 3-D building points, yielding a set of boundary points for each building (Fig. 3d).

2) *Building extraction from optical image*: First, the optical visible image is converted into the CIE $L^*a^*b^*$ color space, since this color space allows a better distinction of objects

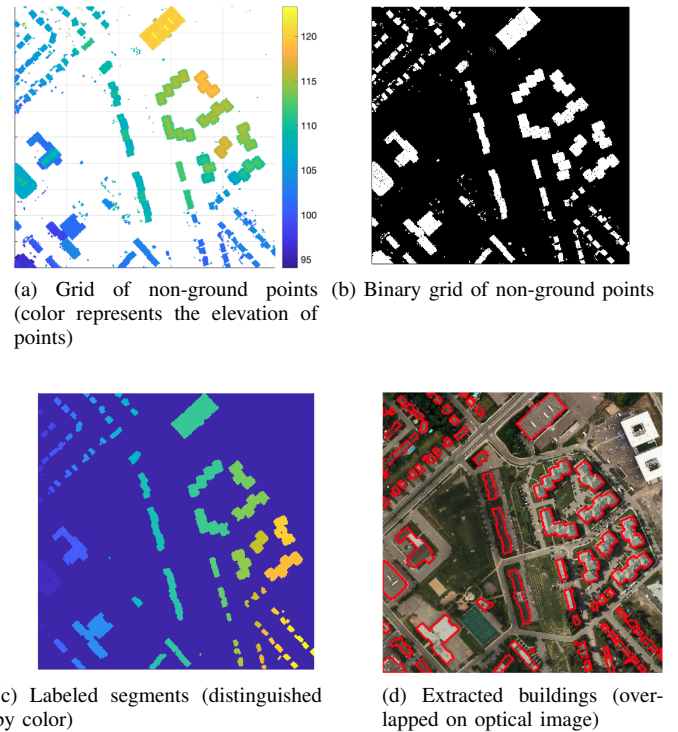


Fig. 3. Illustration of different steps of the building extraction from LiDAR data.

than RGB color space [47]. In this paper, we propose to use mean shift [44] to segment building regions from optical image of an urban area. This technique is more efficient than a k -means clustering since the color of building roofs can vary a lot and some roofs have similar color as streets or surrounding areas. Compared to k -means, mean shift does not require any prior number of classes, but a value of bandwidth corresponding to the image color range and size of objects to be segmented. However, determining the best bandwidth parameter for mean shift still remains difficult despite many investigated approaches [48]. Thus, this parameter should be set adaptively according to the type of urban area (either residential, industrial, mixed, etc.), and the size of objects of interest. In other words, there is a need for a contextualization to set up the mean shift parameter. This contextualization is carried out according to meaningful information in the observed area, such as the estimated number of buildings

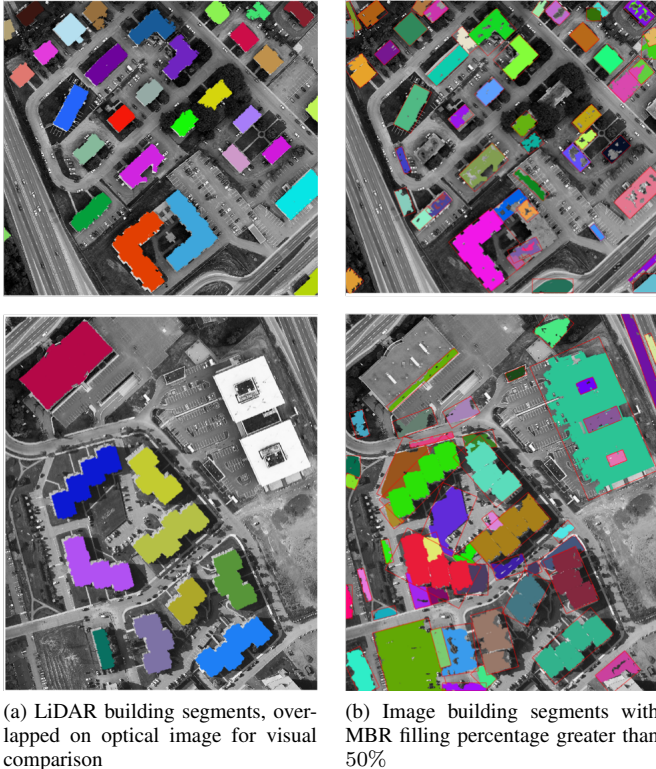


Fig. 4. Illustration of building extraction from LiDAR point cloud and from optical image.

and their relative distances (this information stems from the LiDAR data, cf. III-A1), as well as the resolution and the color range of the optical image. Future works will investigate the automation of this step.

Once the mean shift segmentation is performed, a refinement of the extracted segments is carried out. First, we compute the size of the segments and remove small ones, since they usually correspond to trees and cars. Large segments corresponding to street regions are similarly removed. This filtering is simple and efficient [49], but depends on the image resolution. Therefore, it needs a manual intervention to be set correctly. In this paper, we propose to remove segments whose area is smaller than 800 pixels or larger than 80,000 pixels (equivalent to 18 square meters and 1,800 square meters, respectively). Second, we identify the Minimal Bounding Rectangle (MBR) [50] of each of the remaining segments and calculate, using Eq. (1), the percentage of their area over the area of the MBR.

$$\%_{\text{MBR_filling}} = \frac{\text{area}(\text{segment})}{\text{area}(\text{MBR})} \times 100 \quad (1)$$

This percentage is used to filter the unwanted segments, as filling percentage of a rectangle building segment should be higher than that of an unwanted segment. In this paper, a fixed threshold of 50% of the MBR filling percentages is chosen.

3) *Graph-based matching of extracted segments*: The two sets of buildings extracted from the LiDAR and optical image datasets are taken into consideration and matched. Regarding the optical image, only the segments having a higher percentage than the fixed threshold are considered as stated in

the previous point. On the other hand, all building regions extracted from the LiDAR point cloud are taken into consideration. An example of the two sets of extracted segments are depicted in Fig. 4. A visual comparison of the LiDAR building segments overlapping on the optical image show some errors and issues. These errors and issues were expected since the datasets are relatively distant to each other. In addition, tree/grass segments wrongly extracted as buildings may still remain after the MBR-based segment refinement (cf. Fig. 4b). Therefore, matching the segments based on their relative position with respect to their neighbors is more relevant than comparing their individual values, e.g. area, shape similarity, and so on.

A common pattern connecting the centers of neighboring building segments representing their relative spatial arrangement on both datasets is determined using the Graph Transformation Matching (GTM) algorithm [51]. GTM is a graph-based point matching algorithm designed for non-rigid registration between images. This algorithm performs better than RANSAC [52] for removing *outlier*, i.e. wrongly paired buildings in our context (cf. Table III).

In practice, both GTM and RANSAC require an initial one-to-one matching of segment centers, which can be carried out relying on the positions of vertically projected 3-D building region centers onto plan $z = 0$ and the centers of 2-D segments extracted by mean shift segmentation. In the specific case of satellite imagery and LiDAR data where the relative shifts are large (i.e. approximately up to 40 meters), this initial matching is guided by a translation vector. It is calculated based on the shift of the largest segment in the area. The largest segment is determined relying on the segment absolute area value and its relative area value with respect to other segments.

Result of the segment matching is shown in Fig. 5. Fig. 5a presents the initial matching using segment centers. As we could expect, a number of wrongly paired buildings (i.e. outliers) result from the initial matching. They are originated from tree or grass segments extracted as buildings, or buildings that existed on one dataset but not on the other one. These outliers are then removed using GTM. Fig. 5b depicts the result of GTM, while Fig. 5c presents the result of RANSAC. Finally, as we have considered only the relative position of the segment centers, a refinement of false positives from GTM result is carried out based on the area value and the direction of segments. Taking into account the pairs of segments provided by GTM, only the pairs of segments having a segment area difference lower than 15%, and a segment direction difference lower than 2° are preserved. Other pairs of segments that do not satisfy these criteria are removed. The result of this refinement is presented by Fig. 5d.

Also, the capability of GTM to cope with high percentage of outliers, theoretically up to 75% [51], is also advantageous when handling the registration of datasets that were acquired within a large timespan, e.g. several years. This temporal variability can result in significant changes in urban area, such as construction or deconstruction of buildings.

4) *Global transformation model estimation*: Then, the coordinates of the matched building segment centers are used to estimate the transformation model, which is a finite projective

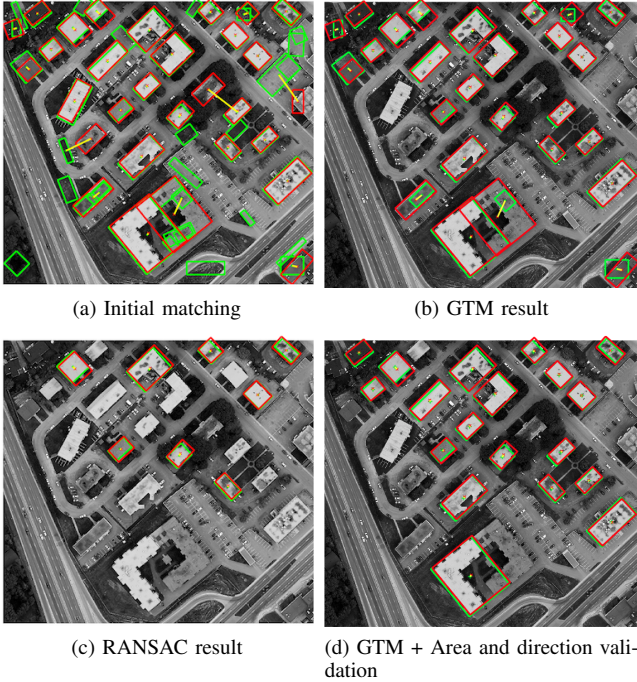


Fig. 5. Matching of building segment centers by considering their relative position. Green and red rectangles represent the MBR of the segments extracted from, respectively, optical image and LiDAR point cloud. Yellow lines connect the centers of the matched segments.

camera model [53]. The transformation from 3-D homogeneous coordinates to 2-D homogeneous coordinates is given by the following 3×4 camera matrix,

$$P = KR[I \ | \ -C] \quad (2)$$

where K is the camera calibration matrix, R stands for the rotation matrix describing the orientation of the camera, I is the identity matrix, and C denotes the coordinates of the camera center. These matrices from Eq. (2) are defined as follows,

$$K = \begin{bmatrix} \alpha_x & s & p_x \\ 0 & \alpha_y & p_y \\ 0 & 0 & 1 \end{bmatrix} \quad (3a)$$

$$C = [X_0 \ Y_0 \ Z_0]^T \quad (3b)$$

$$R = R_z(\kappa)R_y(\phi)R_x(\omega) \quad (3c)$$

where R_x, R_y, R_z are the rotation matrices for rotations around x -, y - and z -axis.

As presented by Eq. (3), the transformation model involves eleven degrees of freedom, related to internal and external parameters of the camera. The internal parameters are the scale factors in the x - and y -coordinate direction α_x and α_y , the skew parameter s and the coordinates of the principal point (p_x, p_y) in terms of pixel dimensions. On the other hand, the external parameters are the position (X_0, Y_0, Z_0) and the orientation (ω, ϕ, κ) of the camera when the image was acquired. The set of all these parameters of the camera pose is denoted by vector θ in what follows.

The external parameters of the camera pose can be measured by the GPS/IMU system. However, it is still necessary to

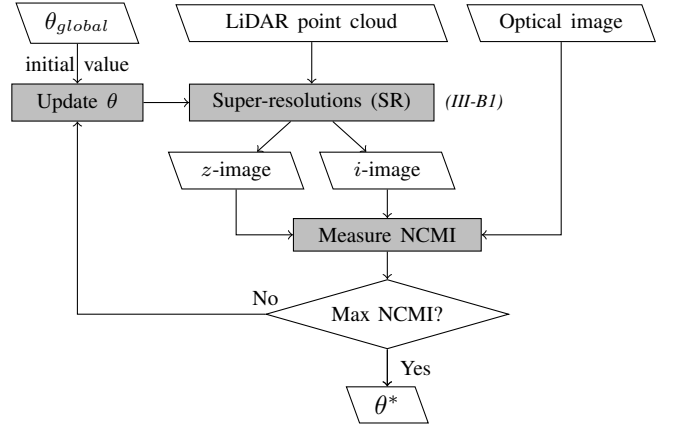


Fig. 6. Flowchart of the proposed fine registration between optical image and LiDAR point cloud.

reestimate them, since the image can suffer from radiometric and geometric errors, as well as undergo an orthorectification process. Based on the coordinates of the resulting matched building segment centers, a transformation model is estimated using Gold Standard algorithm [53, p.187]. We denote the set of parameters associated with this estimated global transformation model by θ_{global} .

B. Fine Registration

After coarsely repositioning the datasets, the next step is dedicated to register them precisely. An area-based optimization approach is relevant in the present context, in order to determine the optimal set of parameters that enables the most accurate registration [16], [17]. However, this approach involves several constraints, such as the datasets need to be spatially close to each other, as well as to have the same resolution and display similar intensity characteristics. As a result of the presented coarse registration and the SR process detailed in the next sub-section (III-B1), these constraints are fulfilled.

We propose a fine registration method, summarized by Fig. 6, which involves a SR applied on the LiDAR data. Then, an estimation of local transformation models is performed based on the maximization of the NCMI or MI measured between the optical image and the *high-resolution* LiDAR-based images, resulted from the SR. The high-resolution term means that these images have the same resolution and size as the optical image. NCMI achieves its maximum values when the images are geometrically aligned [17], yielding an optimal set of camera pose parameters, denoted by θ^* . We detail these points in what follows.

1) *Super-resolution of LiDAR data*: LiDAR point cloud is usually significantly subsampled compared to the optical image. Thus, we propose a process of transferring and propagating values from LiDAR point cloud onto the frame of the optical image, in order to facilitate an area-based registration between them. This subsample problem is usually addressed by a sparse reconstruction (e.g. for pansharpening [54]) or a super-resolution of low-resolution depth maps [55]. In this paper, the aim of this process is to generate a rasterized dataset

with the same size and resolution as the optical image, thus it is called super-resolution. Pixels of the super-resolved image contain the values derived from LiDAR 3-D points, i.e. altitude values or laser return intensity values. The super-resolved image of LiDAR-derived altitude values is called the z -image, whereas the image of intensity values is called i -image.

a) *Mathematical notation:* Inputs of the SR process are the LiDAR point cloud, a transformation model, the frame of reference and the size of the optical image. We denote the optical image by $u \in \mathbb{R}^{n_x \times n_y \times 3}$, where n_x and n_y are respectively the number of rows and columns of the image. The LiDAR point cloud is represented by $\psi \in \mathbb{R}^{m \times 4}$, with m is the number of LiDAR points. Each point contains three spatial coordinates (x, y, z) and a laser return intensity value i . Also, we use $\psi^z \in \mathbb{R}_+^m$ to denote the column of altitude values of the LiDAR points; whereas $\psi^i \in \{0, 1, \dots, 255\}^m$ stands for the intensity value of LiDAR points. For the sake of simplicity, we use the same notation ϕ to denote the result of the SRs, i.e. the z -image and i -image. During the process, ϕ is vectorized into a column vector of $n = n_x \times n_y$ elements.

b) *Transferring of LiDAR values:* Fig. 7 describes the principle of the proposed SR. First, LiDAR values, i.e. altitude and laser return intensity values, are transferred onto the frame of the optical image using the transformation model associated with camera pose parameters θ . At the first iteration of the fine registration, θ is given by θ_{global} obtained from the coarse registration. Mathematically, the value transfer is presented as follows,

$$\phi_{\Omega^*} = H_{\Omega^*} \psi^z \text{ or } \phi_{\Omega^*} = H_{\Omega^*} \psi^i \quad (4)$$

where Ω^* and Ω denote, respectively, the subsets containing the indices of pixels from ϕ , having or not an associated altitude value (or intensity value) transferred from ψ . Thus, ϕ_{Ω^*} and ϕ_{Ω} , respectively, denote the sub-vector containing the pixels with and without a transferred altitude (or intensity) value; whereas ϕ denotes the vector containing all pixels. The dimension of ϕ_{Ω^*} and ϕ_{Ω} , respectively, are $m \times 1$ and $(n - m) \times 1$. The matrix H_{Ω^*} associated to the camera pose parameters θ , is an index matrix allowing to select only the pixels whose values are transferred from the LiDAR point cloud. It is computed based on the projection related to θ (Eq. (2) and (3)) of the LiDAR 3-D point cloud onto the frame of reference of the 2-D optical image. Then, the transferred values are propagated to their neighboring pixels.

c) *Propagation of transferred LiDAR values:* The propagation of transferred values is carried out through the minimization of a cost function $\mathcal{F}(\phi)$, defined by Eq. (5). It is composed of the sum of squared directional gradients (SSDG) of ϕ , and an \mathcal{L}^1 -norm term to promote the sparsity of ϕ , subjecting to the values transferred from the point cloud (described by Eq. (4)).

$$\begin{aligned} \hat{\phi} &= \arg \min_{\phi} \mathcal{F}(\phi) \\ \text{with } \mathcal{F}(\phi) &= \underbrace{\|\nabla_x \phi\|_2^2 + \|\nabla_y \phi\|_2^2}_{f_{SSDG}(\phi)} + \lambda \|\phi\|_1, \quad (5) \\ \text{subject to } \phi_{\Omega^*} &= H_{\Omega^*} \psi^z \text{ or } \phi_{\Omega^*} = H_{\Omega^*} \psi^i \end{aligned}$$

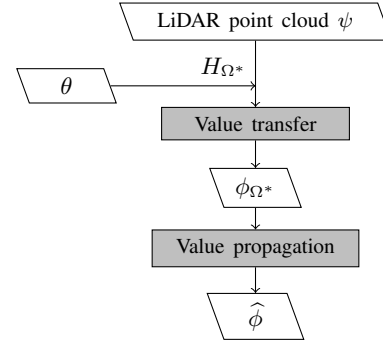


Fig. 7. Overview of the super-resolution process, to generate a high-resolution LiDAR-based image (z - or i -image).

Algorithm 1 Solving Eq. (5) by FISTA algorithm with constant step size γ .

input:

- sparse image ϕ^{spa} ($\phi_{\Omega^*}^{spa} = H_{\Omega^*} \psi^z$ or $\phi_{\Omega^*}^{spa} = H_{\Omega^*} \psi^i$, $\phi_{\Omega}^{spa} = 0$)
- a maximum number of iterations k_{max}
- step size $\gamma > 0$
- soft thresholding parameter $\lambda > 0$
- a tolerance value ϵ

set: $k \leftarrow 1, t_0 \leftarrow 1, y^{(0)} \leftarrow \phi^{spa}$

repeat

$$x_{\Omega}^{(k)} = \mathcal{T}_{\lambda\gamma} \left(y_{\Omega}^{(k-1)} - \gamma H_{\Omega} \nabla f_{SSDG} \left(y^{(k-1)} \right) \right)$$

$$t_k = \frac{1}{2} \left(1 + \sqrt{1 + 4t_{k-1}^2} \right)$$

$$y_{\Omega}^{(k)} = x_{\Omega}^{(k)} + \left(\frac{t_{k-1} - 1}{t_k} \right) \times \left(x_{\Omega}^{(k)} - x_{\Omega}^{(k-1)} \right)$$

$$k \leftarrow k + 1$$

until $k > k_{max}$ **or** $|y^{(k)} - y^{(k-1)}| < \epsilon$

set: $\hat{\phi}_{\Omega^*} \leftarrow \phi_{\Omega^*}^{spa}$ **and** $\hat{\phi}_{\Omega} \leftarrow y_{\Omega}^{(k)}$

output: dense image $\hat{\phi}$

where $\|\cdot\|_p$ stands for the \mathcal{L}^p -norm, ∇_x and ∇_y represent the directional gradient operators along the x - and y -axis.

Our SR approach is inspired by the work of Castonera *et al.* [56]. However, they proposed a cost function that is solely defined by SSDG for the fusion of terrestrial LiDAR data with optical imagery. It relies on a hypothetical characteristic of a depth-map, namely that the magnitude and occurrence of depth discontinuities inside a depth-map should be minimum. The advantages of using this cost function is its convexity and ease to compute. This method also showed good results in propagating depth values across homogeneous regions. However, the mentioned hypothetical characteristic is not suitable in an airborne context, where structures like buildings always exhibit strong elevation discontinuities. These discontinuities should be preserved during and after the super-resolution process, and not being gradually flattened. Therefore, the \mathcal{L}^1 -norm term is additionally proposed in our approach, in order to promote sparsity of the z -image, i.e. preserving elevation discontinuities.

d) *Propagation algorithm*: The optimization problem described by Eq. (5), containing the term $\|\phi\|_1$, can be solved iteratively. Each iteration involves calculating the gradient descent of the SSDG term (i.e. ∇f_{SSDG}) followed by a shrinkage/soft-threshold step. The shrinkage operator $\mathcal{T}_\alpha : \mathbb{R}^n \rightarrow \mathbb{R}^n$ is defined as follows,

$$\mathcal{T}_\alpha(x) = (|x| - \alpha)_+ \times \text{sign}(x) \quad (6)$$

where $(|x| - \alpha)_+ = \max(|x| - \alpha, 0)$, and α is a threshold value, which is set to $\alpha = \lambda\gamma$ in Algorithm 1.

Algorithm 1 presents the process of solving (5), using the Fast Iterative Shrinkage-Thresholding algorithm (FISTA) [57] with a constant step size. In this Algorithm, the superscript (k) of a vector denotes its state at the k -th iteration. The sub-vector x_{Ω^*} (and y_{Ω^*}) contains only the values of pixels indexed by Ω^* , i.e. the pixels having a LiDAR transferred value. They remain unchanged during the SR process. On the other hand, x_Ω (and y_Ω) represents the sub-vector containing the values of pixels indexed by Ω , i.e. the null-valued pixels before the value propagation. A vector ϕ without an index subscript indicates that the vector contains all pixels, i.e. $\phi = \phi_{\Omega \cup \Omega^*}$. For instance, ϕ^{spsa} represents the sparse image where pixels of index in Ω^* are transferred from LiDAR data, while other pixels (i.e. the one of index from Ω) are null-valued.

FISTA with its computational simplicity is adequate for solving large-scale problems and also converges more quickly than ISTA, with a rate of $O(1/k^2)$ [57]. The convergence rate of the SRs is depicted in Fig. 8. Indeed, Fig. 8a and 8c, respectively, depict the errors between the estimated z -images and i -images at two consecutive iterations, i.e. $\|\phi^{(k+1)} - \phi^{(k)}\|_2$. The values of the cost function $\mathcal{F}(\phi^{(k)})$ through iterations are shown in Fig. 8b and 8d. We can observe that after approximately 600 iterations, the estimated z -image and i -image have nearly converged into a stable solution.

Lastly, Fig. 9 shows the results of a transfer and propagation of altitude and intensity values from the LiDAR data onto the frame of the optical image. The value transfer result is depicted through the sparse images, while the value propagation result is demonstrated by the dense images. On the sparse and dense z -images, the pixel color represents the altitude in meters. On the other hand, pixel color on the i -images represents the intensity value between 0 and 255. Using the reference optical image on the same urban scene Fig. 9e provides a visual quality assessment of the super-resolved images. On one hand, we can observe that the elevation of buildings and other objects (e.g. trees, cars, power lines, etc.), as well as the relief of the urban scene are well presented on the dense z -image (Fig. 9c), and correspond with the information in the optical image. On the other hand, different elements of the scene like buildings, grasses, or roads can be discriminated on the i -image, similarly on the optical image. For example, several regions with distinctive elements are highlighted by red ellipses on Fig. 9d and 9e.

2) *Estimation of local transformation model*: As aforementioned, a MI-based registration method involves many constraints. One of them is that it requires the to-be-registered images to have the same resolution. The solution to this prob-

lem is to use high-resolution LiDAR-based images generated by the presented SR approach.

a) *Proposed approach*: This paper presents a MI-based registration method that relies on the MI measured between the optical image and the high-resolution i -image. A NCMI-based registration method is also proposed. It involves measuring the NCMI between the optical image and both high-resolution LiDAR-based z -image and i -image. Both similarity measures, MI and NCMI, are expected to achieve their maximum value when the images (i.e. the optical image and the LiDAR-based image(s)) are geometrically aligned [17], [58].

Moreover, the proposed fine registration also consists in a local approach of transformation model estimation. It involves dividing the study area into many patches of same size and estimating a local transformation model for each patch. Such a patch-based MI optimization allows to accelerate the optimization process [21]. For each patch of the optical image u_t and the LiDAR data ψ_t ($1 \leq t \leq T$, with T is the total number of patches), the determination of the optimal set of camera pose parameters, denoted by θ_t^* , is carried out based on the maximization of MI or NCMI, as follows,

$$\theta_t^* = \arg \max_{\theta \in \Theta} \text{MI}(f_{\text{SR}}^i(\theta, \psi_t); u_t) \quad (7)$$

$$\theta_t^* = \arg \max_{\theta \in \Theta} \text{NCMI}((f_{\text{SR}}^i(\theta, \psi_t), f_{\text{SR}}^z(\theta, \psi_t)); u_t) \quad (8)$$

Equations (7) and (8) present the optimizations based, respectively, on MI and NCMI. f_{SR}^i and f_{SR}^z represent the SR process that generates, respectively, the i -image and z -image (denoted by ϕ from the previous sub-section III-B1), given the camera pose parameters θ and the LiDAR data ψ_t .

In fact, given two random variables A and B with marginal probability density functions (pdfs), $p_A(a)$ and $p_B(b)$ and joint pdf $p_{AB}(a, b)$. Mutual information between A and B , denoted by $\text{MI}(A; B)$, measures the degree of dependence of A and B by measuring the distance between the joint pdf $p_{AB}(a, b)$ and the pdf associated with the case of complete independence $p_A(a).p_B(b)$. This probabilistic distance is expressed by the means of the Kullback-Leibler divergence measure [59], given by Eq. (9),

$$\begin{aligned} \text{MI}(A; B) &= \sum_{a,b} p_{AB}(a, b) \log \frac{p_{AB}(a, b)}{p_A(a).p_B(b)} \\ &= H(A) + H(B) - H(A, B) \end{aligned} \quad (9)$$

where $H(X) = -\sum_x p_X(x) \log p_X(x)$ is the *Shannon entropy* of random variable X . Its estimation is proposed by MokkaDem in [60]. The registration method based on the maximization of MI is originally introduced by [58]. Since then it has been extensively studied in many research areas, particularly to register an optical image with an image derived from LiDAR data. This image is either the LiDAR-derived the DSM or the intensity image, which has the same resolution with the optical image [11], [21].

Another statistical similarity measurement used for the registration between LiDAR data and optical imagery (Eq. (8)) is the Normalized Combined Mutual Information (NCMI) [17], given by Eq. (10).

$$\text{NCMI}((A, B); C) = \frac{H(A, B) + H(C)}{H(A, B, C)} \quad (10)$$

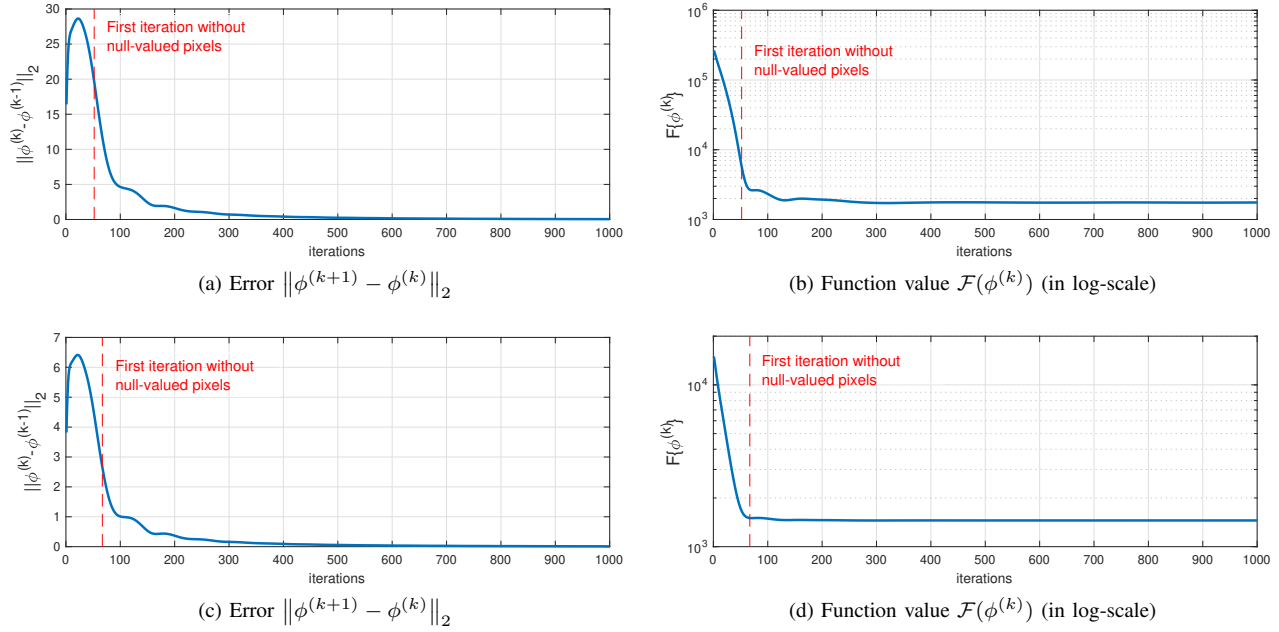


Fig. 8. Errors $\|\phi^{(k+1)} - \phi^{(k)}\|_2$ and cost function values $\mathcal{F}(\phi^{(k)})$ displayed as a function of iterations. Vertical red-dashed lines represent the first iteration where every pixels of the estimate image is filled. First row: from the SR process of generating z -image; second row: from the SR process of generating i -image.

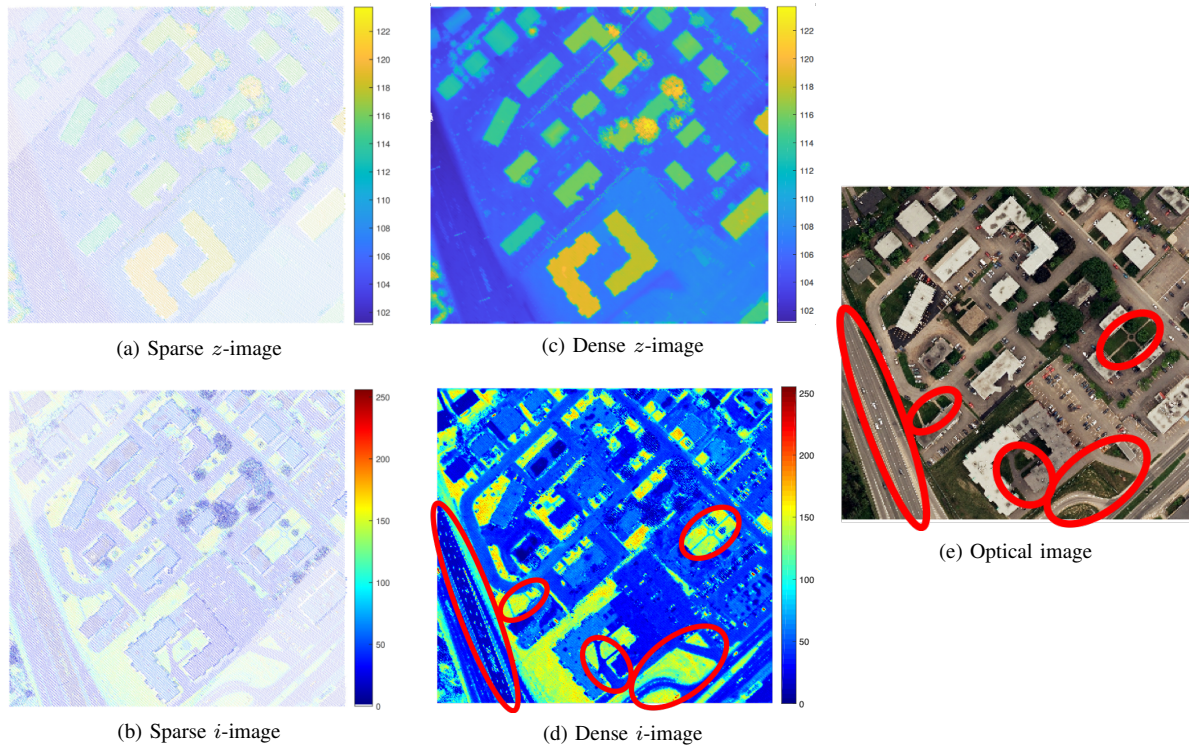


Fig. 9. Examples of super-resolution results. First column: the sparse z -image and i -image from the value transfer process; second column: the dense z -image and i -image from the value transfer and propagation process; third column: the optical image of the same scene for the sake of comparison.

NCMI-based registration method relies on the similarity between the optical image and both LiDAR images, i.e. DSM and intensity image which are inherently registered. This combined similarity measurement is demonstrated to be more informative than the conventional MI [61].

The authors of [11] compared the three usages of LiDAR-

derived images in MI-based registration involving measuring its/their similarity with the optical image, i.e. (i) using only the DSM image, (ii) using only the intensity image, (iii) using both images. They demonstrate that the usage of the intensity image yields more accurate registration result than using the DSM image. The usage of both images is also shown to yield

more accurate result than the two individual usages [17].

b) Implementation: To resolve (7) and (8) we use Nelder-Mead simplex algorithm [62]. This algorithm is derivative-free and also straightforward in terms of implementation. Initial values for the optimization are given by the θ_{global} , resulted from the coarse registration (presented in sub-section III-A).

In this paper, the considered urban area is divided uniformly into patches, of which the size is empirically chosen as 500×550 pixels. The division of the area into patches is irrespective of the distribution of buildings, or in other words, independent of the distribution of primitives used in the coarse registration, illustrated by Fig. 10a. The result of the local transformation model estimation is depicted in Fig. 10b. On each patch, the maximized value of MI between the optical imagery and LiDAR data is displayed, as well as the variations of θ_t^* compared to θ_{global} .

Also, Table II summarizes the evolution of the resulting MI measurements between the global transformation model (i.e. the coarse registration) and the local transformation model (i.e. the fine registration) on each patch. Considering this evolution and taking into account how the primitives are distributed between patches (Fig. 10a), we observe a difference of MI gain between the patches that include many correspondences (i.e. extracted and matched buildings) and the patches that do not. Indeed, on Table II, the MI gains of patches that have zero to one primitive are highlighted in bold letters, whereas the other patches with three to four primitives are in normal letters. This difference emphasizes the interest of the optimization-based registration on the area with very few or no primitives. It compensates for the coarse registration (in terms of MI) which is less effective on these areas than on an area with many primitives.

TABLE II
EVOLUTION OF MI FROM THE COARSE REGISTRATION TO THE FINE REGISTRATION.

Patch (row, column)	# of corre- spondences	MI(θ_{global})	MI(θ_t^*)	$\frac{MI(\theta_t^*)}{MI(\theta_{global})} - 1$
(1,1)	3	0.615	0.661	7.4%
(1,2)	3	0.546	0.583	6.7%
(1,3)	4	0.479	0.542	13.1%
(2,1)	0	0.572	0.662	15.8%
(2,2)	3	0.532	0.584	9.6%
(2,3)	3	0.409	0.507	23.9%
(3,1)	0	0.393	0.666	69.4%
(3,2)	1	0.700	0.817	16.7%
(3,3)	1	0.329	0.640	94.5%
Average	-	0.504	0.629	24.8 %

3) Smoothing of patch-based registration results: A potential problem that can be expected from this patch-based registration approach is the incoherence of local pose parameters θ_t^* between patches. In this regard, it is important to elaborate how the transformation model differs from one patch to another, and particularly how it behaves in transition region between patches.

As we can see on Fig. 10b, the variation of camera external parameters are displayed in relation to the values estimated from the coarse registration, i.e. the global parameters θ_{global} . These variations are quite different from one patch to another

without any noticeable common pattern. Therefore, potential incoherences between them can be expected. As a matter of fact, Fig. 11 illustrates two examples where the difference of transformation models of patches causes a conflict (Fig. 11a) and a discontinuity (Fig. 11b) of projected points on transition regions between patches. In these regions, there are 3-D points which are spatially neighboring but belong to two adjacent patches. Consequently, they are projected with two different transformation models, hence causing a conflict or a discontinuity. However, such problem has not yet been addressed by existing work that presented similar patch-based approach [21].

In this paper, we present a smoothing of camera pose parameters from the locally optimized transformation models. Instead of using the transformation model of a patch for the projection of every points in this patch, we propose to compute the projection of each 3-D point based on a weighted average of several neighboring local transformation models. We denote the center of neighboring patches by C_i , and the local transformation model of patches by θ_i , $i = 1, \dots, N$ where $N = 9$ is the number of neighboring patches of a point p . The transformation model for the point p , denoted by $\theta(p)$, is interpolated using the Inverse Distance Weighting (IDW) [63] average of neighboring local transformation models, given by Equation (11).

$$\theta(p) = \begin{cases} \frac{\sum_{i=1}^N w_i \theta_i}{\sum_{i=1}^N w_i}, & \text{if } d(p, C_i) \neq 0 \\ \theta_i, & \text{if } d(p, C_i) = 0 \end{cases} \quad (11)$$

The weights w_i are calculated by the inverse squared Euclidean distance from the considered point p to neighboring patch centers C_i , as follows,

$$w_i = \frac{1}{d(p, C_i)^2}, i = 1, \dots, N \quad (12)$$

Fig. 11c and 11d depict the resolution of the mentioned incoherence problem between patches, using the IDW-based interpolation of locally optimized camera pose parameters.

IV. QUANTITATIVE RESULTS AND DISCUSSION

Experiments have been carried out to evaluate the quality of the registration and determine whether it is good enough to be beneficial to a subsequent fusion, or to an application. However, the lack of a ground truth, i.e. true values of the camera pose parameters, makes such an evaluation difficult. To overcome this problem, Mastin *et al.* [11] proposed to use expert-chosen control points to determine these values. Otherwise, without a ground truth, the registration quality of existing methods can be assessed through these following manners:

- (i) Using subjective quality indicator or by visual assessment: e.g. a *good assignment of 3-D point-to-pixel on the colorized point cloud* [15, Sec. 3], or assessing whether *the images are close enough for the projective texture mapping* [11], or based on how well the representations of objects (e.g. buildings, vegetation, etc.) align.

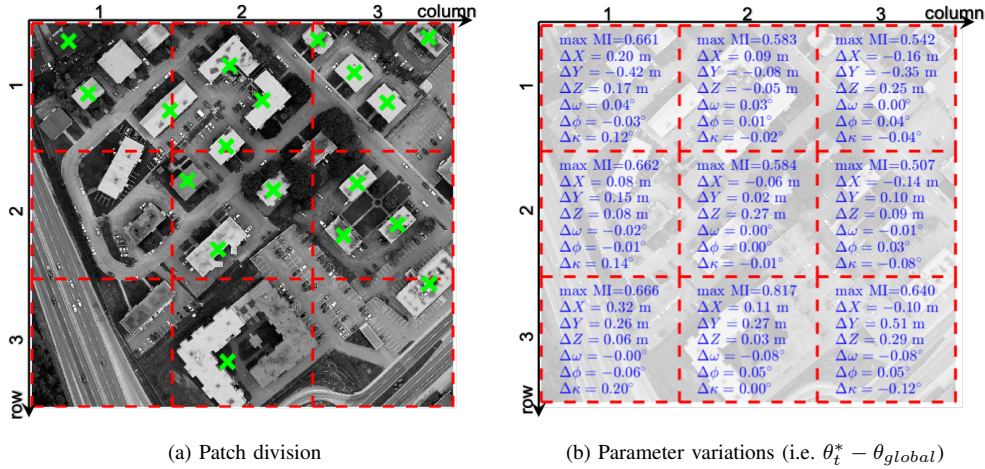


Fig. 10. Illustration of the local transformation model estimation. (a) Division of a considered urban area into patches. Red dashed lines depict the patch boundaries, whereas green 'x' represent the correspondences (i.e. matched primitives) from the coarse registration. (b) Values displayed in each patch are: first row: maximized MI value; other rows: variation of external parameters of the camera pose (i.e. $\theta_t^* - \theta_{global}$).

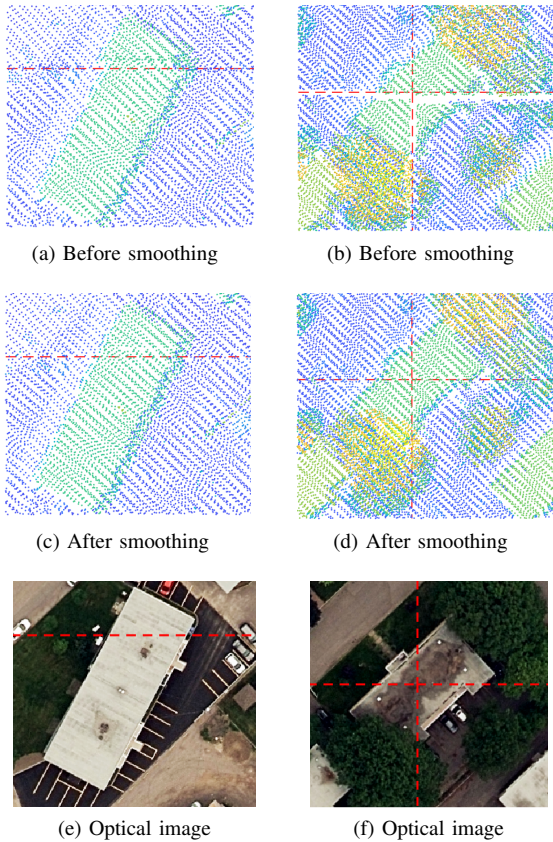


Fig. 11. Examples of (a) a conflict of projected points, and (b) a discontinuity of projected points between neighboring patches, and the results (c) and (d) on the same transition regions after the smoothing using IDW-based interpolation. The red dashed lines represent the patch boundaries. Optical images (e) and (f) of the considered areas are displayed for the sake of comparison. As such, the shapes of the exemplified buildings are well retrieved after the smoothing.

- (ii) Using the average spatial discrepancy between datasets measured at manually determined check points, or using check pair lines.
- (iii) Involving a determination of an optimal set of parameters

that minimizes a cost function (or maximizes a statistical dependency measurement). In other words, a registration is considered successful when the determined parameters are optimal. The cost function can be the MI or its variation between the optical image and the LiDAR intensity image [11], [17], [21]. It can also be defined by the pixel-wise distances calculated between the hyperspectral image and the image derived from LiDAR data using a ray-tracing module [16].

Since a thorough quality evaluation of a registration method is still missing, we present multiple evaluations in this paper. Firstly, an evaluation of building candidate extraction and matching steps from the coarse registration is carried out. Secondly, since our proposed registration method already involves a maximization of MI between datasets for determining optimal camera pose parameters, we perform subsequently two spatial discrepancy evaluations. They are based on (i) check points which are the centroids of manually determined building roofs, and (ii) check pair lines manually sketched from datasets.

In this paper, our proposed registration method is evaluated on two selected urban areas of representative characteristics in Quebec City, QC, Canada. The specifications of the datasets, two optical imagery and two LiDAR datasets, have been presented in Table I. The optical images consist of an orthorectified aerial image acquired in 2016 and a Pliades satellite image acquired in 2015 (columns 1 and 2 of Table I). The LiDAR datasets consist of airborne LiDAR point clouds acquired in 2011 and 2017 (columns 3 and 4 of Table I). The two selected urban areas are depicted in Fig. 12. The first area is composed of mostly planar roof buildings and relatively close to each other. On the other hand, the second area is composed of big buildings and gable roof houses. Particularly in this area, there are two buildings at the top left corner of Fig. 12b that were not built in 2011, namely the year when one of the LiDAR dataset was recorded. On each area, four registrations have been performed and evaluated.

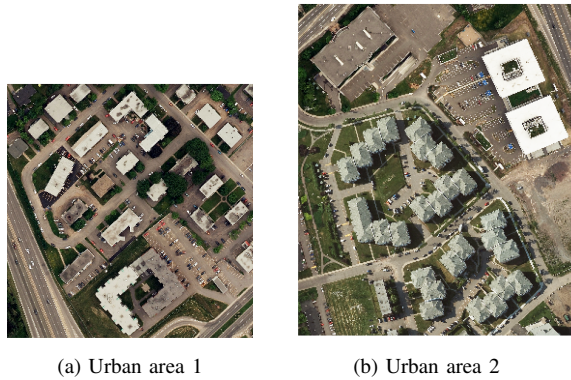


Fig. 12. Two selected urban areas representing by orthorectified aerial image, on which we evaluate the registration method. The first urban area is composed of 28 buildings over 0.06 square kilometers; whereas the second urban area is composed of 12 buildings over 0.1 square kilometers.

A. Evaluation of building candidate extraction and matching steps

Table III summarizes the quantitative results of building extraction and matching on the selected areas. The performance metrics are the number of true positives (TP), false alarms (FA), and misses (M). In the context of the building extraction, a TP indicates that a building is correctly extracted, whereas a FA represents a non-building segment incorrectly extracted as building, and M means that a building exists but is not extracted. On the other hand, in the context of segment matching, a TP indicates a good match, a FA represents an incorrectly matched pair of segments, whereas M means a pair of segments that should be matched are not paired. The Precision and Recall metrics are computed as follows, $\text{Precision} = \text{TP}/(\text{TP} + \text{FA})$ and $\text{Recall} = \text{TP}/(\text{TP} + \text{M})$.

TABLE III
PERFORMANCE OF BUILDING EXTRACTIONS AND MATCHING ALGORITHMS ON SELECTED AREAS

	Extracted from LiDAR data	Extracted from image by mean shift	Matching result by RANSAC	Matching result by GTM
TP/FA/M	28/0/0	24/21/4	8/0/12	19/7/1
Precision	100%	53.33%	100%	73.08%
Recall	100%	85.71%	40%	95%

(a) On selected area 1 with 28 buildings in total

	Extracted from LiDAR data	Extracted from image by mean shift	Matching result by RANSAC	Matching result by GTM
TP/FA/M	10/0/0	11/37/1	7/1/2	9/1/0
Precision	100%	22.92%	87.5%	90%
Recall	100%	91.67%	77.78%	100%

(b) On selected area 2, there are in total 12 buildings, but before 2013 there were only 10.

Visual results of the building extraction from LiDAR data (2011) and from aerial optical image (2016) are depicted in Fig. 4. On the one hand, as highlighted in Table III, the building extraction from LiDAR data (both 2011 and 2017) has achieved 100% of precision and recall thanks to the contribution of 3-D information. On the other hand, the mean

shift segmentation and segment refinement have yielded very high number of TPs (e.g. 24 over 28 buildings on the first area are extracted) but also a high number of FAs (i.e. 21 segments are incorrectly extracted as buildings). This number is even higher on the second area, i.e. 37 FAs.

Then considering the matching step, despite yielding relatively high precision (i.e. 100% on the first area and 87.5% on the second one), RANSAC provides a very low number of TPs and a high number of misses. GTM outperforms RANSAC on both areas, yielding more correct matches of building segments. Nevertheless, on the first area, it yields a 95% of recall, with a relatively high number of FAs (i.e. 7 segment pairs are wrongly matched). These FAs are then eliminated by the subsequent validation based on segment area and direction (cf. Fig. 5).

B. Spatial discrepancy evaluation

The second evaluation focuses on assessing the registration through the spatial discrepancy between the datasets. In this regard, we propose to use manually determined check points (i.e. centroids of building roofs) and check pair lines (i.e. mainly building straight boundaries). They are determined from the optical image, and the high-resolution z -image generated from LiDAR point cloud. Indeed, in order to estimate the spatial discrepancy of datasets before registration, a z -image is generated using the presented SR process with an orthographic projection (i.e. vertical projection) of LiDAR point cloud. For the coarse registration, another z -image is generated using the global transformation model given by θ_{global} . Finally, in order to assess the spatial discrepancy after fine registration (either MI or NCMI), the optimal transformation model is used to generate the z -image. In the two following assessments, we propose to use z -image instead of i -image for these assessments, since it allows a better manual determination of building roofs and building boundary line segments (cf. Fig. 9c and 9d).

1) *Based on centroids of building roofs:* The first evaluation is carried out based on centroids of building roofs. The distance (in meters) between the centroids of each pair are measured. A smaller distance indicates a more precise registration. Table IV presents the spatial discrepancy evaluation between LiDAR data (2011) and LiDAR data (2017) with orthorectified aerial imagery (2016), and then the spatial discrepancy evaluation between LiDAR data (2011) and LiDAR data (2017) with the Pliades multispectral imagery data (2015). The gain values are computed based on average spatial discrepancy value after registration with respect to the value before registration.

a) *Between orthorectified aerial image and LiDAR data:* Considering the orthorectified aerial image (2016), as a result of the image orthorectification, the average discrepancy between this data set and the airborne LiDAR dataset (both 2011 and 2017) has already been relatively small, i.e. respectively 1.05 and 1.04 meters. Table IV shows that our proposed registration yields an even smaller discrepancy. Indeed, the proposed coarse registration method results in a reduction of these values by approximately 50%. This reduction highlights the effectiveness of repositioning the datasets closer to each

TABLE IV
BUILDING REGION CENTROIDS-BASED SPATIAL DISCREPANCY EVALUATION.

	LiDAR data (2011) and aerial imagery (2016)			LiDAR data (2017) and aerial imagery (2016)			LiDAR data (2011) and Pliades imagery (2015)			LiDAR data (2017) and Pliades imagery (2015)		
	Mean	(Std)	Gain	Mean	(Std)	Gain	Mean	(Std)	Gain	Mean	(Std)	Gain
Before registration	1.08	(0.52)	-	1.05	(0.68)	-	42.89	(1.47)	-	44.43	(1.73)	-
Coarse registration	0.56	(0.30)	48.15%	0.54	(0.55)	48.57%	2.06	(1.24)	95.20%	1.39	(0.44)	96.87%
MI-based fine registration	0.46	(0.29)	57.41%	0.43	(0.32)	59.05%	1.41	(0.78)	96.71%	1.20	(0.58)	97.30%
NCMI-based fine registration	0.40	(0.27)	62.96%	0.35	(0.31)	66.67%	0.99	(0.45)	97.69%	0.82	(0.45)	98.15%
Gain of using NCMI over MI	13.04%			18.60%			29.79%			31.66%		

other. Then, a spatial discrepancy of 40 cm between LiDAR data (2011) and orthorectified aerial imagery (2016), and of 35 cm between LiDAR data (2017) and orthorectified aerial imagery (2016) are provided by the proposed coarse-to-fine registration method.

It is worth noting that both the LiDAR datasets acquired in 2011 and 2017 involve a horizontal accuracy of nearly 17 cm. The resulting discrepancy values, respectively 40 and 35 cm, are slightly bigger than the combination of horizontal accuracy of the orthorectified aerial imagery and airborne LiDAR data which are respectively 16.5 cm and 17 cm (cf. Table I).

Also, the reported average discrepancy between LiDAR data (2011) and orthorectified aerial imagery (2016) after the registration is also slightly bigger than 1/2 of the average point spacing of the considered LiDAR point cloud (i.e. 70 cm). On the other hand, regarding the registration between LiDAR data (2017) and the orthorectified aerial imagery (2016), the resulting average discrepancy approximates the average point spacing of the LiDAR point cloud (i.e. 35.4 cm).

b) Between Pliades image and LiDAR data: The discrepancy evaluation of the registration between the airborne LiDAR data (2011 and 2017) and the Pliades imagery (2015) can be analyzed similarly from the results presented at the third and fourth columns of Table IV. The utilized optical image is a 50-centimeter resolution multispectral image, resulted from a pansharping [64] of a 50-centimeter resolution panchromatic image and a 2-meter resolution multispectral image. More importantly, the horizontal accuracy of Pliades image is theoretically between 1 and 3 meters, depending on the usage of ground control points on the considered area. These two characteristics of Pliades imagery data, especially the horizontal accuracy, are the major factors causing its registration with LiDAR data (both 2011 and 2017) to be not as accurate as the registration between LiDAR data and aerial image (2016). When regarding the resulting average discrepancy (i.e. 0.99 and 0.82 meters) and taking into account the spatial resolution of the datasets (i.e. 50 cm for the imagery data and 70 cm/35.4 cm for LiDAR point spacing), one may interpret that these results are not good enough. However, as the horizontal accuracy of the Pliades imagery dataset varies between 1 to 3 meters as aforementioned, we would argue that such average registration discrepancy results are highly desirable.

Comparing the MI-based and the NCMI-based fine registra-

tion, a gain averaging approximately 23% is achieved when using NCMI instead of MI. However, it is worth noting that the NCMI-based fine registration takes twice as long as the MI-based, since it involves performing the SR twice, for the z -image and the i -image. Therefore, the use of both statistical similarity measurements shows promising beneficial result. And the decision that which one of them should be used is essentially a compromise between accuracy and computational cost of the registration method.

Overall, the proposed coarse-to-fine method yields a very significant reduction of the spatial discrepancy between datasets, namely 63% to 67% for the registration of LiDAR data and orthorectified aerial imagery, and 98% for the registration of LiDAR data and Pliades imagery.

2) Based on check pair line segments: The authors of [18] proposed an evaluation based on distances between line segments that are manually sketched from the two datasets, before and after the registration. Compared with check point-based evaluation, this evaluation relies on a higher geometrical basis (i.e. line segments compared with points) to assess of the registration. A smaller distance indicates a more precise registration. The distance proposed in [18] between two line segments p (with A and B are its end-points) and q is defined as follows,

$$d(p, q) = \frac{1}{2}(d_A + d_B) \quad (13)$$

where d_A and d_B respectively denote the distances from A and B to the line segment q . However, this distance given by Eq. (13) is not relevant, because it yields small values when the two line segments are far away but close to be collinear. Based on the literature review of line segment distances [65], the Hausdorff line segment distance [66] is more suitable for this evaluation. It measures the longest of all the distances from a point on one line segment to the other segment, and it equals zero only if the two line segments are identical, i.e. same two end-points. Thus, it reflects fairly the discrepancy between two line segments, even when they intersect or are collinear.

In our experiment, two sets of seventy-two line segments have been manually sketched on the optical image and on the generated LiDAR-based high-resolution z -image. They are then manually matched, yielding check pair line segments. The source for these line segments are mainly building straight boundaries. The Hausdorff distances between each pair is computed. A smaller distance indicates a more precise registration.

TABLE V
CHECK PAIR LINE-BASED SPATIAL DISCREPANCY EVALUATION.

	LiDAR data (2011) and aerial imagery (2016)			LiDAR data (2017) and aerial imagery (2016)			LiDAR data (2011) and Pliades imagery (2015)			LiDAR data (2017) and Pliades imagery (2015)		
	Mean	(Std)	Gain	Mean	(Std)	Gain	Mean	(Std)	Gain	Mean	(Std)	Gain
Before registration	1.19	(0.67)	-	1.08	(0.80)	-	44.61	(0.74)	-	44.68	(2.02)	-
Coarse registration	0.95	(0.83)	20.17%	0.81	(0.32)	25.00%	2.01	(0.39)	95.49%	2.18	(1.00)	95.12%
MI-based fine registration	0.64	(0.30)	45.82%	0.67	(0.29)	37.96%	1.95	(0.65)	95.63%	1.92	(1.25)	95.70%
NCMI-based fine registration	0.64	(0.29)	45.95%	0.63	(0.26)	41.67%	1.47	(0.61)	96.70%	1.21	(0.33)	97.29%
Gain of using NCMI over MI	2.33%			5.97%			24.62%			36.98%		

Table V summarizes the quantitative results of check pair line-based evaluation of the registrations between airborne LiDAR data (2011 and 2017) with orthorectified aerial imagery (2016), and with the Pliades multispectral imagery data (2015).

As we can see from Table V, the discrepancy between datasets measured based on manually sketched line segments is significantly reduced after each of the registration, i.e. the coarse and the fine registration. On the one hand, the proposed registration method ultimately yields an average discrepancy of 0.63 and 0.64 meters between LiDAR data (2017 and 2011) and the orthorectified aerial imagery (2016). On the other hand, for the registration of LiDAR data (2017 and 2011) and the Pliades multispectral imagery (2015), the resulting check pair line-based discrepancy value is 1.21 and 1.47 meters. However, it is important to remind the principle of Hausdorff distance in order to evaluate the discrepancy results. For example, we consider two nearly identical horizontal line segments (parallel to x -axis), having same first end-point, and the second end-point of one line segment is 4 pixels away from the second end-point of other line segment (pixel size: 15 centimeters). Consequently, the resulting Hausdorff distance between them is 60 centimeters. Therefore, it should be noted that the mentioned discrepancy values yielded by our proposed method are relatively small. Overall, over all four registrations, the check-pair-line-based discrepancy vary between 3 and 4 pixels.

Overall, a discrepancy reduction of approximately 42% to 46% is achieved on the registration between the airborne LiDAR data (2011 and 2017) and the orthorectified aerial imagery (2016). Similarly, a spatial discrepancy reduction of approximately 97% (96.70% and 97.29%) is benefited from the registration between the airborne LiDAR data (2011 and 2017) and the Pliades multispectral imagery (2015).

Finally, it is worth noting that, in the registration between the airborne LiDAR data and the Pliades multispectral imagery, the benefit of the NCMI-based fine registration compared to MI-based fine registration is much more evident. Based on both check point-based and check pair line-based evaluation result, using NCMI-based fine registration instead of MI-based results in average gains of 30.7% and 30.8% of spatial discrepancy reduction. The first percentage is computed from check point-based evaluation result (cf. last row of Table IV), whereas the second percentage is computed from check pair line-based evaluation result (cf. last row of Table V). On the other hand, for the registration between the airborne

LiDAR data and the orthorectification aerial image, these gains are only 15.8% and 4.15%.

Both spatial discrepancy evaluations and all these mentioned elements show that the results yielded by our proposed method are decent and relevant.

V. CONCLUSIONS AND PERSPECTIVES

This paper has presented and evaluated a coarse-to-fine registration method between airborne LiDAR data and optical imagery. It is dedicated to overcome the challenges associated with the difficult context, where the two datasets are not acquired from the same platform, neither from the same point of view nor having the same spatial resolution, and level of detail.

First, a coarse feature-based registration is carried out based on the extraction and matching of building region candidates on both datasets, reducing significantly the spatial shift between them. Then, a fine registration based on a maximization of MI or NCMI (both measures have been performed separately) is carried out to determine the optimal camera pose, granting the datasets to be precisely aligned. It involves a process of super-resolution of LiDAR data to generate high-resolution images of altitude and intensity values respectively. This approach neutralizes the difference of spatial resolution and level of detail between datasets. Thus it enables the MI-based and NCMI-based fine registration between these datasets. The fine registration also involves dividing the considered area into many small patches. For each patch a local transformation model is estimated. This approach allows to reduce significantly the computational cost of the optimization-based method. Lastly, a smoothing of locally optimized transformation models is performed in order to avoid conflicts between them. It is based on an weighted average of camera pose parameters from neighboring patches.

Many elements of the proposed method are intended as the solution to the challenges which are associated with the considered context. First, in order to address the spatial shift between datasets caused by the differences in point of view and field of view, a coarse registration is carried out. It relies on using buildings as primitives, which is a relevant choice of primitive considering the low density of airborne LiDAR point cloud around vertical surfaces. Then, spatial resolution and levels of detail differences between datasets have been dealt with by the SR approach. An optimization-based fine registration using MI/NCMI measurements is carried out to

finely tune the optimal local transformation model. Overall, as highlighted by different spatial discrepancy assessments, the proposed method has achieved a very high registration accuracy. It is highly desirable, especially when taking into account the difficulties of the considered context, and the horizontal accuracy of datasets.

It is suggested by the authors of [16] that only one registration approach is not sufficient to accurately register data from heterogeneous sensors, even when they are rigidly fixed to the same platform. In this paper, we proposed a coarse-to-fine registration method consisted of two steps of registration. The proposed registration method also reinforces the relevance of a coarse-to-fine approach for registering an optical aerial/satellite imagery with an airborne LiDAR dataset. Nevertheless, the proposed registration method still has limitations in a natural environment, such as forest or desert areas, due to the lack of man-made objects providing reliable primitives. The registration between LiDAR data and optical image on these environments will be studied in the future for an effective solution. Finally, with these promising results, the reported research has established a basis for a comprehensive fusion of aerial/satellite optical imagery and airborne LiDAR data in future researches.

ACKNOWLEDGMENT

This work was co-funded by the Natural Sciences and Engineering Research Council of Canada and the Brittany region (France). The authors also would like to thank Centre GéoStat, Université Laval (QC, Canada), as well as Québec City, Communauté Métropolitaine de Québec (QC, Canada), and Centre National d'Études Spatiales (France) for providing the datasets used in this work.

We also would like to thank Dr. Hongchao Ma, School of Remote Sensing and Information Engineering, Wuhan University, China for his/her help on the usage of the check-pair line evaluation.

REFERENCES

- [1] H. B. Mitchell, *Multi-sensor data fusion: an introduction*. Springer Science & Business Media, 2007.
- [2] M. Dalla Mura, S. Prasad, F. Pacifici, P. Gamba, J. Chanussot, and J. A. Benediktsson, "Challenges and opportunities of multimodality and data fusion in remote sensing," *Proceedings of the IEEE*, vol. 103, no. 9, pp. 1585–1601, 2015.
- [3] E. P. Baltsavias, "A comparison between photogrammetry and laser scanning," *ISPRS Journal of Photogrammetry and Remote Sensing*, vol. 54, no. 2-3, pp. 83–94, 1999.
- [4] M. Awrangjeb, M. Ravanbakhsh, and C. S. Fraser, "Automatic detection of residential buildings using lidar data and multispectral imagery," *ISPRS Journal of Photogrammetry and Remote Sensing*, vol. 65, no. 5, pp. 457–467, 2010.
- [5] N. Longbotham, F. Pacifici, T. Glenn, A. Zare, M. Volpi, D. Tuia, E. Christophe, J. Michel, J. Inglada, J. Chanussot *et al.*, "Multi-modal change detection, application to the detection of flooded areas: Outcome of the 2009–2010 data fusion contest," *IEEE Journal of Selected Topics in Applied Earth Observations and Remote Sensing*, vol. 5, no. 1, pp. 331–342, 2012.
- [6] T. H. Nguyen, D. Gueriot, J.-M. Le Caillec, C. Sintès, and S. Daniel, "Heterogeneous data registration for 3d underwater scene reconstruction," in *OCEANS–Anchorage, 2017*. IEEE, 2017, pp. 1–6.
- [7] P. Ghamisi, B. Rasti, N. Yokoya, Q. Wang, B. Hofle, L. Bruzzone, F. Bovolo, M. Chi, K. Anders, R. Gloaguen *et al.*, "Multisource and multitemporal data fusion in remote sensing: A comprehensive review of the state of the art," *IEEE Geoscience and Remote Sensing Magazine*, vol. 7, no. 1, pp. 6–39, 2019.
- [8] A. Wehr and U. Lohr, "Airborne laser scanning—an introduction and overview," *ISPRS Journal of photogrammetry and remote sensing*, vol. 54, no. 2-3, pp. 68–82, 1999.
- [9] J. B. Campbell and R. H. Wynne, *Introduction to remote sensing*. Guilford Press, 2011.
- [10] T. H. Nguyen, S. Daniel, D. Gueriot, C. Sintès, and J.-M. Le Caillec, "Unsupervised automatic building extraction using active contour model on unregistered optical imagery and airborne lidar data," *arXiv preprint arXiv:1907.06206*, 2019.
- [11] A. Mastin, J. Kepner, and J. Fisher, "Automatic registration of LIDAR and optical images of urban scenes," *2009 IEEE Computer Society Conference on Computer Vision and Pattern Recognition Workshops, CVPR Workshops 2009*, pp. 2639–2646, 2009.
- [12] M. Khodadadzadeh, J. Li, S. Prasad, and A. Plaza, "Fusion of hyperspectral and lidar remote sensing data using multiple feature learning," *IEEE Journal of Selected Topics in Applied Earth Observations and Remote Sensing*, vol. 8, no. 6, pp. 2971–2983, 2015.
- [13] C. Debes, A. Merentitis, R. Heremans, J. Hahn, N. Frangiadakis, T. van Kasteren, W. Liao, R. Bellens, A. Pižurica, S. Gautama *et al.*, "Hyperspectral and lidar data fusion: Outcome of the 2013 GRSS data fusion contest," *IEEE Journal of Selected Topics in Applied Earth Observations and Remote Sensing*, vol. 7, no. 6, pp. 2405–2418, 2014.
- [14] M. Campos-Taberner, A. Romero-Soriano, C. Gatta, G. Camps-Valls, A. Lagrange, B. Le Saux, A. Beaupère, A. Boulch, A. Chan-Hon-Tong, S. Herbin *et al.*, "Processing of extremely high-resolution lidar and rgb data: Outcome of the 2015 IEEE GRSS data fusion contest—part a: 2-d contest," *IEEE Journal of Selected Topics in Applied Earth Observations and Remote Sensing*, vol. 9, no. 12, pp. 5547–5559, 2016.
- [15] A.-V. Vo, L. Truong-Hong, D. Laefer, D. Tiede, S. d'Oleire Oltmanns, A. Baraldi, M. Shimoni, G. Moser, and D. Tuia, "Processing of extremely high resolution lidar and rgb data: outcome of the 2015 IEEE GRSS data fusion contest—part b: 3-d contest," *IEEE Journal of Selected Topics in Applied Earth Observations and Remote Sensing*, vol. 9, no. 12, pp. 5560–5575, 2016.
- [16] M. Brell, C. Rogass, K. Segl, B. Bookhagen, and L. Guanter, "Improving sensor fusion: A parametric method for the geometric coalignment of airborne hyperspectral and lidar data," *IEEE Transactions on Geoscience and Remote Sensing*, vol. 54, no. 6, pp. 3460–3474, 2016.
- [17] E. G. Parmehr, C. S. Fraser, C. Zhang, and J. Leach, "Automatic registration of optical imagery with 3D LiDAR data using statistical similarity," *ISPRS Journal of Photogrammetry and Remote Sensing*, vol. 88, pp. 28–40, 2014. [Online]. Available: <http://dx.doi.org/10.1016/j.isprsjprs.2013.11.015>
- [18] S. Peng, H. Ma, and L. Zhang, "Automatic registration of optical images with airborne lidar point cloud in urban scenes based on line-point similarity invariant and extended collinearity equations," *Sensors*, vol. 19, no. 5, p. 1086, 2019.
- [19] R. Cura, J. Perret, and N. Paparoditis, "A scalable and multi-purpose point cloud server (pcs) for easier and faster point cloud data management and processing," *ISPRS Journal of Photogrammetry and Remote Sensing*, vol. 127, pp. 39–56, 2017.
- [20] J. Zhang and X. Lin, "Advances in fusion of optical imagery and lidar point cloud applied to photogrammetry and remote sensing," *International Journal of Image and Data Fusion*, vol. 8, no. 1, pp. 1–31, 2017.
- [21] E. G. Parmehr, C. S. Fraser, C. Zhang, and J. Leach, "Automatic registration of optical imagery with 3d lidar data using local combined mutual information," *ISPRS Annals of the Photogrammetry, Remote Sensing and Spatial Information Sciences*, vol. 5, p. W2, 2013.
- [22] B. O. Abayowa, A. Yilmaz, and R. C. Hardie, "Automatic registration of optical aerial imagery to a lidar point cloud for generation of city models," *ISPRS Journal of Photogrammetry and Remote Sensing*, vol. 106, pp. 68–81, 2015.
- [23] S. O. Elberink, "Problems in automated building reconstruction based on dense airborne laser scanning data," *International Archives of Photogrammetry, Remote Sensing and Spatial Information Science*, vol. 37, p. B3, 2008.
- [24] D. Lahat, T. Adali, and C. Jutten, "Multimodal data fusion: an overview of methods, challenges, and prospects," *Proceedings of the IEEE*, vol. 103, no. 9, pp. 1449–1477, 2015.
- [25] R. K. Mishra and Y. Zhang, "A Review of Optical Imagery and Airborne LiDAR Data Registration Methods," *The Open Remote Sensing Journal*, vol. 5, no. 12, pp. 54–63, 2012.
- [26] G. P. Asner, D. E. Knapp, J. Boardman, R. O. Green, T. Kennedy-Bowdoin, M. Eastwood, R. E. Martin, C. Anderson, and C. B. Field, "Carnegie airborne observatory-2: Increasing science data dimensional-

- ity via high-fidelity multi-sensor fusion,” *Remote Sensing of Environment*, vol. 124, pp. 454–465, 2012.
- [27] S. Liu, X. Tong, J. Chen, X. Liu, W. Sun, H. Xie, P. Chen, Y. Jin, and Z. Ye, “A linear feature-based approach for the registration of unmanned aerial vehicle remotely-sensed images and airborne lidar data,” *Remote Sensing*, vol. 8, no. 2, p. 82, 2016.
- [28] R. Wang, “3d building modeling using images and lidar: A review,” *International Journal of Image and Data Fusion*, vol. 4, no. 4, pp. 273–292, 2013.
- [29] A. A. Goshtasby, *Image registration: Principles, tools and methods*. Springer Science & Business Media, 2012.
- [30] J. Lee, X. Cai, C. B. Schönlieb, and D. A. Coomes, “Nonparametric image registration of airborne LiDAR, hyperspectral and photographic imagery of wooded landscapes,” *IEEE Transactions on Geoscience and Remote Sensing*, vol. 53, no. 11, pp. 6073–6084, 2015.
- [31] P. Bunting, F. Labrosse, and R. Lucas, “A multi-resolution area-based technique for automatic multi-modal image registration,” *Image and Vision Computing*, vol. 28, no. 8, pp. 1203–1219, 2010. [Online]. Available: <http://dx.doi.org/10.1016/j.imavis.2009.12.005>
- [32] W. Dorigo, M. Hollaus, W. Wagner, and K. Schadauer, “An application-oriented automated approach for co-registration of forest inventory and airborne laser scanning data,” *International Journal of Remote Sensing*, vol. 31, no. 5, pp. 1133–1153, mar 2010. [Online]. Available: <http://www.tandfonline.com/doi/abs/10.1080/01431160903380581>
- [33] A. Safdarinezhad, M. Mokhtarzade, and M. Valadan Zoej, “Shadow-Based Hierarchical Matching for the Automatic Registration of Airborne LiDAR Data and Space Imagery,” *Remote Sensing*, vol. 8, no. 6, p. 466, 2016. [Online]. Available: <http://www.mdpi.com/2072-4292/8/6/466>
- [34] G. Pandey, J. R. McBride, S. Savarese, and R. M. Eustice, “Automatic targetless extrinsic calibration of a 3d lidar and camera by maximizing mutual information,” in *AAAI*, 2012.
- [35] P. Viola and W. M. Wells III, “Alignment by maximization of mutual information,” *International journal of computer vision*, vol. 24, no. 2, pp. 137–154, 1997.
- [36] T. Schenk, “Fusion of Lidar Data and Aerial Imagery for a More Complete Surface Description,” *International Archives of Photogrammetry Remote Sensing and Spatial Information Sciences*, vol. 34, no. 3/A, pp. 310–317, 2002. [Online]. Available: http://rsl.geology.buffalo.edu/documents/schenk_{_}csatho_{_}graz.pdf
- [37] P. Rönholm and H. Haggren, “Registration of Laser Scanning Point Clouds and Aerial Images Using Either Artificial or Natural Tie Features,” *ISPRS Annals of Photogrammetry, Remote Sensing and Spatial Information Sciences*, vol. 1-3, no. September, pp. 63–68, 2012. [Online]. Available: <http://www.isprs-ann-photogramm-remote-sens-spatial-inf-sci.net/I-3/63/2012/>
- [38] M. Ding, K. Lyngbaek, and A. Zakhor, “Automatic registration of aerial imagery with untextured 3D LiDAR models,” *26th IEEE Conference on Computer Vision and Pattern Recognition, CVPR*, 2008.
- [39] S. Huang, S. Chen, Y. Zhang, P. Guo, and H. Chen, “A multi-scale registration of urban aerial image with airborne lidar data,” in *Selected Papers of the Photoelectronic Technology Committee Conferences held June–July 2015*, vol. 9795. International Society for Optics and Photonics, 2015, p. 979518.
- [40] A. Wong and J. Orchard, “Efficient FFT-accelerated approach to invariant optical-LIDAR registration,” *IEEE Transactions on Geoscience and Remote Sensing*, vol. 46, no. 11, pp. 3917–3925, 2008.
- [41] R. M. Palenichka and M. B. Zaremba, “Automatic extraction of control points for the registration of optical satellite and lidar images,” *IEEE Transactions on Geoscience and Remote sensing*, vol. 48, no. 7, pp. 2864–2879, 2010.
- [42] D. G. Lowe, “Distinctive image features from scale-invariant keypoints,” *International journal of computer vision*, vol. 60, no. 2, pp. 91–110, 2004.
- [43] T. H. Nguyen, S. Daniel, D. Gueriot, C. Sintès, and J.-M. Le Caillec, “Robust Building-Based Registration of Airborne Lidar Data and Optical Imagery on Urban Scenes,” in *IGARSS 2019*. Yokohama, Japan: IEEE GRSS, Jul. 2019. [Online]. Available: <https://hal.archives-ouvertes.fr/hal-02075341>
- [44] D. Comaniciu and P. Meer, “Mean shift: A robust approach toward feature space analysis,” *IEEE Transactions on pattern analysis and machine intelligence*, vol. 24, no. 5, pp. 603–619, 2002.
- [45] S. Gilani, M. Awrangzeb, and G. Lu, “An automatic building extraction and regularisation technique using lidar point cloud data and orthoimage,” *Remote Sensing*, vol. 8, no. 3, p. 258, 2016.
- [46] Z. Chen, B. Gao, and B. Devereux, “State-of-the-art: Dtm generation using airborne lidar data,” *Sensors*, vol. 17, no. 1, p. 150, 2017.
- [47] B. Hill, T. Roger, and F. W. Vorhagen, “Comparative analysis of the quantization of color spaces on the basis of the cielab color-difference formula,” *ACM Transactions on Graphics (TOG)*, vol. 16, no. 2, pp. 109–154, 1997.
- [48] J. E. Chacón and P. Monfort, “A comparison of bandwidth selectors for mean shift clustering,” *arXiv preprint arXiv:1310.7855*, 2013.
- [49] N. L. Gavankar and S. K. Ghosh, “Automatic building footprint extraction from high-resolution satellite image using mathematical morphology,” *European Journal of Remote Sensing*, vol. 51, no. 1, pp. 182–193, 2018.
- [50] H. Freeman and R. Shapira, “Determining the minimum-area enclosing rectangle for an arbitrary closed curve,” *Communications of the ACM*, vol. 18, no. 7, pp. 409–413, 1975.
- [51] W. Aguilar, Y. Frauel, F. Escolano, M. E. Martínez-Pérez, A. Espinosa-Romero, and M. A. Lozano, “A robust graph transformation matching for non-rigid registration,” *Image and Vision Computing*, vol. 27, no. 7, pp. 897–910, 2009.
- [52] M. A. Fischler and R. C. Bolles, “Random sample consensus: a paradigm for model fitting with applications to image analysis and automated cartography,” *Communications of the ACM*, vol. 24, no. 6, pp. 381–395, 1981.
- [53] R. Hartley and A. Zisserman, *Multiple view geometry in computer vision*. Cambridge university press, 2003.
- [54] X. X. Zhu and R. Bamler, “A sparse image fusion algorithm with application to pan-sharpening,” *IEEE transactions on geoscience and remote sensing*, vol. 51, no. 5, pp. 2827–2836, 2013.
- [55] J. Lu and D. Forsyth, “Sparse depth super resolution,” in *Proceedings of the IEEE Conference on Computer Vision and Pattern Recognition*, 2015, pp. 2245–2253.
- [56] J. Castorena, G. Puskorius, and G. Pandey, “Motion guided lidar-camera autocalibration and accelerated depth super resolution,” *arXiv preprint arXiv:1803.10681*, 2018.
- [57] A. Beck and M. Teboulle, “A fast iterative shrinkage-thresholding algorithm for linear inverse problems,” *SIAM journal on imaging sciences*, vol. 2, no. 1, pp. 183–202, 2009.
- [58] F. Maes, A. Collignon, D. Vandermeulen, G. Marchal, and P. Suetens, “Multimodality image registration by maximization of mutual information,” *IEEE transactions on medical imaging*, vol. 16, no. 2, pp. 187–198, 1997.
- [59] I. Vajda, *Theory of statistical inference and information*. Kluwer Academic Pub, 1989, vol. 11.
- [60] A. Makkadem, “Estimation of the entropy and information of absolutely continuous random variables,” *IEEE Transactions on Information Theory*, vol. 35, no. 1, pp. 193–196, 1989.
- [61] N. D. Cahill, “Normalized measures of mutual information with general definitions of entropy for multimodal image registration,” in *International Workshop on Biomedical Image Registration*. Springer, 2010, pp. 258–268.
- [62] J. A. Nelder and R. Mead, “A simplex method for function minimization,” *The computer journal*, vol. 7, no. 4, pp. 308–313, 1965.
- [63] D. Shepard, “A two-dimensional interpolation function for irregularly-spaced data,” in *Proceedings of the 1968 23rd ACM national conference*. ACM, 1968, pp. 517–524.
- [64] S. Rahmani, M. Strait, D. Merkurjev, M. Moeller, and T. Wittman, “An adaptive ihs pan-sharpening method,” *IEEE Geoscience and Remote Sensing Letters*, vol. 7, no. 4, pp. 746–750, 2010.
- [65] S. Wirtz and D. Paulus, “Evaluation of established line segment distance functions,” *Pattern Recognition and Image Analysis*, vol. 26, no. 2, pp. 354–359, 2016.
- [66] H. Alt, B. Behrends, and J. Blömer, “Approximate matching of polygonal shapes,” *Annals of Mathematics and Artificial Intelligence*, vol. 13, no. 3-4, pp. 251–265, 1995.